Hybrid Au-ZnO/(Water-Ethylene Glycol)-Nanofluid Based PV/T Spectral Beam

Sandesh Chougule, Bhagyashree Gaikwad, A. Inbaoli, Anand Ajayan, Sandip Saha, Patrice Estellé

To cite this version:

Sandesh Chougule, Bhagyashree Gaikwad, A. Inbaoli, Anand Ajayan, Sandip Saha, et al.. Hybrid Au-ZnO/(Water-Ethylene Glycol)-Nanofluid Based PV/T Spectral Beam. Energy, 2025, 331, pp.137055. ⟨10.1016/j.energy.2025.137055⟩. ⟨hal-05115905⟩

HAL Id: hal-05115905

https://hal.science/hal-05115905v1

Submitted on 17 Jun 2025

Hybrid Au-ZnO/(Water-Ethylene Glycol)-Nanofluid Based PV/T Spectral Beam Splitter for Efficient Photo-Harvesting

*Sandesh S. Chougule [1, 2] *, Bhagyashree A. Gaikwad [3], Inbaoli A [4], Anand Ajayan [5],*
Sandip K. Saha [6], and Patrice Estellé [2, 7]

[1] *Clean Energy Processes (CEP) Laboratory, Department of Chemical Engineering, Imperial College London, London SW72AZ, United Kingdom*

[2] *Laboratoire de Génie Civil et Génie Mécanique (LGCGM), Université de Rennes, Rennes 35000, France*

[3] *Atharva College of Engineering, Mumbai, Maharashtra-400095, India*

[4] *Department of Mechanical Engineering, National Institute of Technology Calicut, Kerala-673601, India*

[5] *School of Physics, Indian Institute of Science Education and Research (IISER) Thiruvananthapuram, Vithura-Kerala-695551, India*

[6] *Department of Mechanical Engineering, Indian Institute of Technology Bombay, Mumbai- 400076, India*

[7] *University of Science and Technology of Hanoi, Vietnam Academy of Science and Technology, Hanoi, Vietnam*

****Corresponding author:*** *Sandesh S. Chougule*

Email: s.chougule@imperial.ac.uk

Highlights

- Au-ZnO/W NFs were synthesized through a reagent-free, cost-effective electrophoretic method.
- Au-concentration, d_{Au}, t_{opt}, and $\dot{m}$ are the performance matrices chosen for Au-ZnO/(W-EG) NF-based PV/T spectral splitter.
- Au-ZnO/(W-EG)-NF retained 90% absorption (A/A_0) for over 100 h, outperforming ZnO/(W-EG) (<14 h).
- Exceptional η_{th}, η_{el}, and η_{total} obtained through the designed PV/T spectral splitter are 74.24%, 12.9%, and 81.52%, respectively, under different optimized conditions.
- Increasing MF (~ 12.93 %) alongside a decreasing η_{ex} (~ 11.55%) with rising $\dot{m}$ from 2 to 6 mL/min.

Abstract

Persistent challenges in photovoltaic/thermal (PV/T) systems with nanofluids (NFs) arise from colloidal instability, reducing optical absorption and thermal conductivity, which this study addresses through the techno-economic analysis and performance evaluation of a hybrid Au-zinc oxide (ZnO)/(W-EG) nanofluids as a spectral splitter for enhanced photo-harvesting. ZnO nanosheets (NSs) and Au nanoparticles (NPs) were synthesised via a reagent-free electrophoretic method and citrate reduction. The hybrid Au-ZnO/(W-EG) NF, dispersed in a 50:50 W-EG mixture, exhibited a localized surface plasmon resonance (LSPR) peak at 540 nm and UV absorption at 370 nm, reducing UV transmittance to near zero while maintaining 87-97% visible transmittance at 5-50 ppm Au-NP concentrations. Stability tests showed the Au-ZnO/(W-EG) NF retained 90% absorption (A/A_0) for over 100 h, outperforming ZnO/(W-EG) (<14 h). In a PV/T system under 1000 W/m^2 solar irradiance, the NF at 50 ppm achieved a total efficiency (η_{total}) of 76.24% (η_{th}: 64.62%, η_{el}: 11.62%), a 7.42-fold enhancement over 5 ppm (η_{total}: 70.97%), though η_{el} decreased by 7.19% due to reduced transmission. Increasing $\dot{m}$ from 2 to 6 mL/min raised η_{th} from 51.12% to 62.23% and η_{el} from 12.01% to 12.06% (t_{opt}: 10 mm), while larger Au-NP sizes (20 to 60 nm) reduced η_{total} by 6.5% at 5 ppm. The merit function (MF) increased from 1.793 to 2.025 with $\dot{m}$, but η_{ex} decreased from 15.24% to 13.48%, reflecting a trade-off between energy quantity and quality. Overall, this hybrid NF offers superior spectral splitting and stability, positioning it as a promising candidate for advanced photo-harvesting.

Keywords: Au-nanoparticles, Au-ZnO/(W-EG) nanofluids, localized surface plasmon resonance, solar PV/T spectral beam splitter, ZnO nanosheets.

Nomenclature

Abbreviations

BIPVs	building-integrated photovoltaics
c-Si	crystalline silicon
EG	ethylene glycol
HTF	heat transfer fluid
MPP	maximum power point
IR	infrared
I-V	Current-voltage
NP	nanoparticle
NS	nanosheet
NF	nanofluid
PT	photo-thermal
PV	photovoltaic
PV-T	photovoltaic-thermal
PVP	polyvinylpyrrolidone
PEG	polyethylene Glycol
QDs	Quantum dots
SBS	spectral beam splitting
SPR	surface plasmon resonance
UV	ultra-violet
W	water

Symbols

A_{PV}	active area of PV cell (m^2)
Cp	specific heat capacity (J $kg^{-1}K^{-1}$)
d_{NPs}	nanoparticles diameter (nm)
t_{opt}	optical thickness (mm)
G	solar irradiance (W/m^2)
I_{max}	maximum current (Amp)
$\dot{m}$	mass flow rate (kg/s)
MF	Merit function
T_{in}	inlet temperature (°C)
T_{out}	outlet temperature (°C)
T_{amb}	ambient temperature (°C)
T_{nf}	nanofluids temperature (°C)
V_{MAX}	maximum voltage (V)

Greek Letters

η_{el}	PV-T's electrical efficiency (%)
η_{th}	PV-T's thermal efficiency (%)
η_{total}	PV-T's total efficiency (%)
η_{ex}	exergy efficiency (%)
η_{p}	pump efficiency (%)
ω	worth factor

1. Introduction

The escalating global energy crisis and environmental pollution underscore the urgent need for sustainable solutions, with solar energy emerging as a cornerstone for addressing these challenges. Rising energy demands have intensified the push for decarbonization and renewable energy adoption, appealing to a broad audience ranging from policymakers and engineers to environmentally conscious communities [1–3]. Among renewable sources, solar energy stands out due to its minimal environmental footprint, low location dependence, and unlimited availability, making it accessible and relevant to diverse societal needs [4]. PV technology, a rapidly advancing and widely adopted method of harnessing solar power, now dominates renewable energy installations worldwide, driving progress toward carbon neutrality and sustainable development [5]. However, inefficiencies in utilizing the full solar spectrum, particularly the loss of infrared (IR) energy as heat, limits PV performance, a challenge that resonates with researchers, industry professionals, and end-users seeking enhanced efficiency [6].

To address this, PV/T hybrid systems have gained prominence by synergistically combining electrical and thermal energy generation, offering a versatile solution for residential, industrial, and commercial applications [7–10]. Spectral splitting, which selectively directs solar wavelengths, enhances solar energy utilization in these systems by cooling PV cells with a heat transfer fluid (HTF) while enabling simultaneous PV and photothermal (PT) conversion [11–13]. Despite their potential, PV/T systems face limitations, such as thermal output constrained by PV cell operating temperatures, prompting the development of advanced spectral beam splitters (SBS) like thin-film filters and selective absorbers [14,15]. Thin-film filters, made from layered dielectric materials, offer precision but suffer from high costs and complexity, whereas selective absorbers provide cost-effective, integration-friendly alternatives, particularly for building-integrated PV/T (BIPV/T) applications [16,17]. NF-based SBS, such as those pioneered by Chendo and Salawu, with a peak η_{th} of 27.6%, further enhance this technology by tuning optical properties like spectral transmittance through nanoparticle diameter (d_{NPs}), concentration, and optical thickness (t_{opt}) [18-21].

Research on NFs has explored a wide range of materials, from oxides (e.g., ZnO, SiO_2) and metals (e.g., Ag, Au, Cu) to hybrids, revolutionizing PV/T performance. The research highlights the potential of NFs such as polypyrrole/water [22], Cu_9S_5/oleylamine [23], Fe_3O_4/electrolyte [24], ZnO/EG or Ag-ZnO/EG [25,26], and SiO_2/water [27]. Among these, noble metal NFs like silver (Ag) and gold (Au) stand out, leveraging their LSPR for superior optical performance. Ag/water-NF showed promise but experienced delamination at higher concentrations within two weeks. Meanwhile, reduced graphene oxide decorated with silver (rGO-Ag) offered enhanced optical properties and slow stability degradation, making it a compelling candidate for advanced PV/T systems [28–30]. In this quest, Hjerrild et al. [31] demonstrated that Au-nanorods enhanced near-infrared absorption, boosting energy output by 79% for Si-PV cells and 111% for GaAs-PV cells, though Si-PV cells responded poorly to UV-visible light.

Au-NPs, known for their rich optical properties, biocompatibility, and versatile surface chemistry, are widely used in displays, photocatalysis, imaging, and photothermal therapy. Their application as NF-based SBS in solar energy is still emerging [32]. Otanicar *et al.* [33] tested Au/ITO-NF outdoors, finding high UV-visible absorption but limited η_{th} (~ 4%) due to excessive visible light absorption. Li *et al.* [34] also optimised Au/water-NF SBS, achieving η_{el} of 8.72% and exergy efficiency (η_{ex}) of 13.71% exergy efficiency at 20 ppm level of Au-NPs and t_{opt} of 18 mm. Filipe *et al.* [35] developed a theoretical model optimising parameters like t_{opt} and d_{NPs}, achieving a merit function (*MF*) value of 1.30. However, studies often examined these parameters independently, highlighting the need for integrated optimisation for PV/T efficiency. In 2021, Chen et al. [36] systematically investigated 13 different plasmonic materials and identified Cu-SiO_2 (20-30 nm) as the most efficient and cost-effective nanofluid for PV/T applications. As Cu alone can easily oxidize in the air or water, a SiO_2 coating is designed around the Cu NP, which consequently enhances solar absorption. Whereas in another report, they investigated Au-NFs for PV/T performance and showed surface plasmonically enhanced solar absorption efficiency up to 89.38% for 10 ppm concentration and 70 mm optical height [37].

Combining plasmonic metal-NPs with semiconducting metal oxides enhances stability and absorption, leading to efficient PV/T-SBSs. Hjerrild *et al.* [38] in 2016 conducted pioneering lab experiments with water-Ag-SiO_2/carbon NFs in PV/T systems, reporting a 30% improvement in η_{total} through thermal energy generation compensating for electrical losses. Further studies were carried out by He *et al.* [39] in 2019 which highlighted that the efficacy of Ag-TiO_2-NPs in W-EG mixtures, achieving an η_{total} of 83.7% at 1 kW/m² with only 200 ppm concentration. An *et al.* [40] in 2018 found that Au-based core-shell nanostructures (Au-SiO_2) outperformed silver-based NPs (Ag-SiO_2), increasing η_{th} by 6.8% and 4.8%, respectively. In 2018, Yu and Xuan [41] demonstrated a 96.1% instantaneous photo-thermal conversion efficiency for CuO/Ag hybrid NFs at 35 °C, attributing the improvement to the

LSPR of Ag-NPs. Han *et al.* [42] further optimized short-wavelength absorption using Ag/$CoSO_4$-NFs, achieving higher solar-to-electrical and thermal conversion efficiencies than Ag/SiO_2-NFs. Moreover, when the optimised Ag/$CoSO_4$ nanoparticles are dispersed within a propylene glycol [43]. Therefore, low-cost alternatives like ZnO, with its 3.3 eV bandgap, have also shown promise, increasing solar energy conversion efficiency by 3.8% compared to filter-less PV systems [44]. These advancements highlight the adaptability of NF-based SBS to diverse contexts, from high-performance industrial systems to affordable residential solutions. A subsequent experimental investigation of Huang *et al.* [45] revealed silica-coated silver nanoparticles (Ag@SiO_2) nanoparticles, prepared via the hydrolysis of tetraethyl orthosilicate (TEOS) in the presence of dimethylamine as a basic solvent, exhibited a dense, homogeneous silica shell with a thickness of 34 nm and an absorption peak at 474 nm, which closely aligns with the maximum of the solar spectrum. These attributes render the nanoparticles particularly suitable for integration into spectral splitting photovoltaic/thermal (PV/T) systems.

In parallel, several complementary studies have further advanced the field by exploring alternative spectral splitting strategies and optimisation techniques. Ju *et al.* [46] have demonstrated that a comprehensive analysis and optimisation of multiple parameters can further refine the performance of nanofluid spectrum splitting PV/T systems. Their work involved the development and validation of a steady-state numerical model for a double-pass configuration, facilitating a detailed investigation into the impacts of nanofluid parameters such as particle size, concentration, and nanofluid channel thickness together with operating conditions including volume flow rate and concentration ratio. The optimisation results revealed that lower-concentrated illumination conditions necessitated smaller particle sizes and higher concentrations compared with non-concentrated scenarios. For systems operating under low concentration ratios (ranging from 2 to 7), the optimised parameters predominantly featured particle sizes between 30 and 60 nm, concentrations between 50 and 150 ppm, and channel thicknesses from 0.005 to 0.01 m. This investigation underscores the critical role of parameter optimisation in advancing the performance and exergy efficiency of nanofluid spectrum splitting PV/T systems and thus complements the empirical findings described previously. Concurrently, Abdelrazik *et al.* [47] have conducted a numerical investigation into a hybrid PV/optical filtration (PV/OF) system employing a water/silver nanofluid. Through the development of thermal, optical, and electrical models—which were validated against existing experimental data—the study examined the effects of nanoparticle size, loading, channel height, and flow rate under varying atmospheric conditions and solar concentrations. The results demonstrated that the hybrid system outperformed standalone PV modules, particularly at elevated ambient temperatures and higher solar concentration levels, thereby underscoring the potential of optical filtration in mitigating PV cell overheating and enhancing overall energy yield. Elharoun *et al.* [48] have proposed a novel PV/T design that integrates a compound parabolic concentrator (CPC) with a selective absorptive fluid-based optical filter. Their experiments, which evaluated the impact of various air gap widths (1, 3, and 5 cm) between the filter and the PV cell as well as the tilting of the concentrator, revealed that systems equipped with the optical filter demonstrated superior η_{el} of approximately 17% compared to 13.1% for CPC-PV systems without a filter and 7.1% for bare PV cells. Similarly, Xiao *et al.* [49] have introduced a hybrid nanofluid containing antimony tin oxide (ATO) and cupric oxide (CuO) nanoparticles for spectral beam splitting applications. The synergistic combination of ATO's strong infrared absorption and CuO's pronounced ultraviolet/visible light absorption facilitates effective spectral regulation. Their findings indicate that a hybrid nanofluid with a 5:5 ATO:CuO mass ratio and a concentration of 200 ppm achieved a merit function value of 1.679 (for a worth factor of 3), highlighting its competitiveness relative to other metal-based nanofluid systems. Collectively, these studies reinforce the importance of the precise synthesis of functional nanomaterials and the rigorous optimisation of system parameters in advancing the performance and viability of spectral splitting photovoltaic thermal systems. The integration of tailored nanofluids, whether employed as an optical filter or as a component of the spectral beam splitter, not only improves thermal and electrical efficiencies but also increases economic value. This comprehensive approach substantiates the multifaceted benefits of these innovative technologies.

Building on this foundation, this study introduces a novel Au-ZnO/(W+EG)-NF as a highly efficient SBS for PV/T systems, targeting a wide audience seeking sustainable, scalable, and cost-effective energy solutions. Unlike previous works that often-optimized parameters like nanoparticle size or concentration independently (e.g., Li *et al.*'s [26] Au/water-NF with η_{el} of 8.72%, or Filipe *et al.*'s [27] theoretical model with an MF of 1.30) this research integrates plasmonic Au NPs and semiconducting ZnO NSs in a water + ethylene glycol (W+EG) suspension. This dual-material design enhances spectral splitting efficiency, stability, and thermal management, distinguishing it from single-material NFs (e.g., Chen *et al.*'s Cu-SiO_2 or Au-H_2O systems [29]) that face oxidation or cost barriers. On the other hand, nanofluid-based PV/T systems suffer from colloidal instability, broadband absorption reducing spectral selectivity, and high costs [22]. This study introduces a hybrid Au-ZnO/(W-EG) NF, leveraging

Au NPs' LSPR and ZnO NSs' UV absorption to achieve >76% efficiency and >144 h stability, addressing these critical gaps with a scalable, cost-effective solution. Through systematic analysis of optical properties, particle dispersion, and concentration-dependent behaviour, this work achieves superior solar energy management, validated by rigorous experimental assessments of η_{th} and η_{el}. By maximizing solar spectrum utilization, this innovation reduces fossil fuel reliance, lowers greenhouse gas emissions, and promotes energy equity, aligning with global sustainability goals and setting a new standard in renewable energy technology.

2. Materials and Experimental Details

2.1. Synthesis of Au-ZnO/(W+EG) NF

The materials employed for the preparation of the Au-ZnO/water nanofluid (NF) is presented in supplementary materials. The 60 nm ± 5 nm Au NPs were specifically chosen due to their superior balance of LSPR absorption characteristics, spectral alignment, and prolonged colloidal stability. Unlike smaller nanoparticles (<20 nm), which rapidly aggregate in W-EG mixtures and exhibit a blue-shifted LSPR (~520 nm), the 60 nm size maintains enhanced visible transmittance and sustained stability over extended periods (>144 h), aligning closely with solar spectrum peaks.

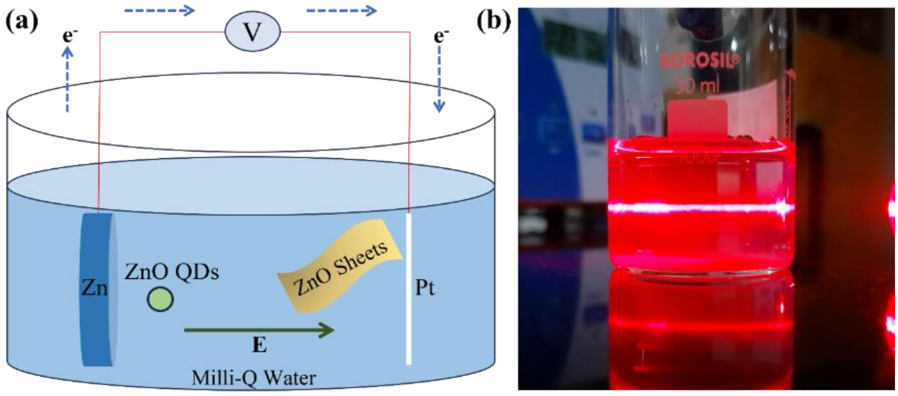

Fig. 1. (a) Experimental setup for synthesising ZnO NSs through reagent-free electrophoretic setup consisting of Zn-pellets and Pt electrode, (b) real-time image of Au-ZnO NF showing Tyndall effect.

The synthesis of the Au-ZnO/(W-EG)-NF was carried out in two sequential steps. Initially, ZnO NSs were synthesised through a reagent-free electrophoretic method using a zinc pellet and platinum wire as electrodes [50]. To ensure optimal performance, the zinc pellet was polished meticulously to eliminate any surface oxide layers prior to the reaction. Then, these ZnO-NSs were dissolved in Milli-Q water and EG solvent in 1:1 volume ratio, showing good stability of the NF and increased absorption in the UV region, which agrees well with the literature [51]. Further, pre-synthesised Au NPs were mixed into the ZnO NSs solution in Milli-Q water and EG solvent system to complete the preparation of Au-ZnO/(W-EG)-NF.

Au-NPs were synthesised via the citrate reduction method introduced by Tyagi *et al*. [52]. A 2.2 M sodium citrate solution in 150 mL of double-distilled water was heated in a round-bottom flask with vigorous stirring for 15 min, using a condenser to prevent solvent evaporation. Upon boiling, 1 mL of 25 mM $HAuCl_4$ was added, causing a colour change from golden yellow to bluish grey, indicating gold seed formation. The solution was cooled to 90 °C, and 1 mL of $HAuCl_4$ was injected continuously for 30 min to promote seed growth. Then mixture was diluted with 53 mL of water and 2 mL of 60 mM sodium citrate, followed by further $HAuCl_4$ injection to control NP size. This method yielded monodisperse citrate-stabilized Au NPs in water.

Table 1. Tabulation of the various selected parameters to optimize the electrophoresis synthesis of ZnO NSs.

Sample Name	**V_{apl} (V)**	**I_{max} (µA)**	**Time (h)**	**Electrode Separation (cm)**	**Volume (mL)**
S1	10	105	1	1	27
S2	10	105	1	1.5	40
S3	10	105	2	1	27
S4	10	105	3	1	27
S5	10	92.3	3	1.5	20
S6	10	105	4	1	27
S7	10	105	5	1	27
S8	10	105	5	2	27
S9	10	105	11	2	27
S10	20	105	1	1	23
S11	20	105	7.6	1	23

The experimental setup shown in Fig. 1(a) was optimised for ZnO NSs synthesis by varying reaction time (1-11 h), electrode spacing (1-2 cm), and voltage (10-20 V), with parameters detailed mentioned in Table 1. In electrophoretic synthesis, anisotropic ZnO NSs align with the electric field due to induced dipole moments, concentrating near electrodes and increasing local particle density. This promotes van der Waals-driven agglomeration, reducing stability (zeta potential: -30 mV to -15 mV). Sample S9, synthesized under optimal conditions (11 h, 10 V, and 2 cm electrode spacing), was selected for further study due to its lowest UV transmittance. Structural confirmation was achieved via the Tyndall effect (Fig. 1(b)), where light scattering makes the beam path visible in a colloidal solution, which aligns with the literature [53,54].

2.2. Experimental Setup

A spectral-splitting PV/T system with a rectangular Ag-ZnO/(W-EG)-NF PV/T filter was designed to study $\eta_{th}$and η_{el}, as shown in Fig. (2). The setup included a solar simulator, a PV/T unit, an electrochemical workstation for PV data acquisition, and photo-thermal data acquisition, temperature sensors and parasitic pumps, etc. The Ag-ZnO/(W-EG)-NF absorbed solar energy at unused wavelengths, transferring heat to the fluid and allowing suitable light to reach the PV cell. Temperature sensors monitored the inlet and outlet variations for thermal efficiency, while current-voltage (I-V) data assessed power output and heat dissipation. The spectral-splitting PV/T system with an Ag-ZnO/(W-EG) NF absorber operates through a well-coordinated mechanism to optimise both thermal and electrical energy conversion.

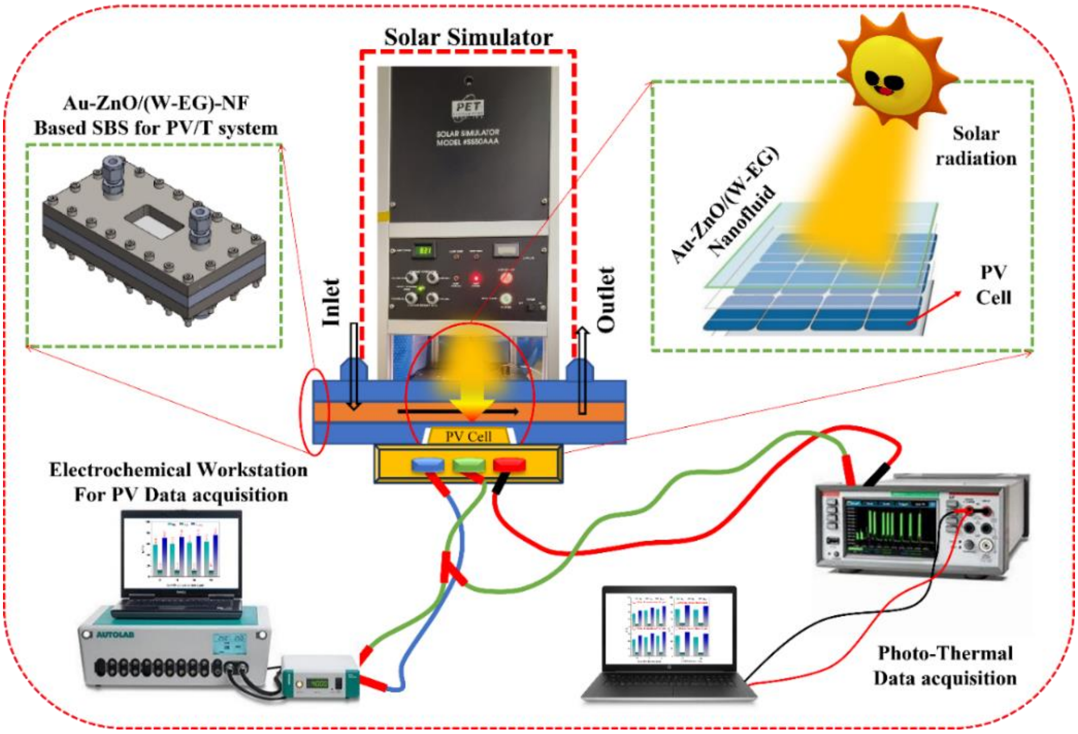

Fig. 2. Schematic experimental arrangement of Au-ZnO/(W-EG)-NF-based SBS system for PV/T study.

The Ag-ZnO/(W-EG) NF selectively absorbs solar energy at wavelengths not utilised by the PV cell, allowing only the appropriate wavelengths to pass through and strike the PV cell's surface. This ensures effective utilisation of the solar spectrum. As the NF absorbs excess solar energy, its temperature rises, and the heated fluid is pumped into a separate beaker via a peristaltic pump, isolating the captured thermal energy. To monitor the thermal process, digital temperature sensors are installed at the inlet and outlet of the nanofluid filter system, measuring the temperature variation and enabling precise calculation of thermal efficiency. Simultaneously, the PV cell generates electricity from the transmitted light, and its performance is evaluated by recording I-V characteristics and operating temperature using an I-V tracer. The collected data from the temperature sensors and I-V tracer is then used to assess the system's overall performance, calculating both thermal and electrical efficiencies. This integrated setup allows the PV/T system to perform dual functions: harnessing thermal energy for heating applications and converting optimised light into electricity. This synergy of thermal management and electricity generation enhances the overall energy efficiency of the system.

2.3. Performance Matrices of Au-ZnO/(W-EG)-PV/T System

Electrical (η_{el}) and thermal (η_{th}) efficiencies are the dominant parameters for the Au-ZnO/(W-EG) PV/T System, while exergy efficiency (η_{ex}) gauges output energy quality. An *MF* with an adjustable worth factor (ω) adapts to different economic conditions, enhancing versatility. Herein, a few key indices are extracted from the measured data in order to analyse the performance of the Au-ZnO/(W-EG) NF based spectral splitting PV/T system.

2.3.1. Photothermal Efficiency

Generally, two theoretical models are assessed η_{th}across different PV/T modules. The key step involved linking the NFs' absorbed energy to the filter's accepted radiation. Therefore, an instant η_{th}model was used as given by

$$\eta_{th} = \frac{\dot{m}\, C_p (T_{out} - T_{in})}{A_{pv}\, G\, \Delta t} \tag{1}$$

where, $\dot{m}$ is the mass flow rate (kg/s), C_p is the specific heat (J/ Kg K), T_{in} and T_{out} are the inlet and outlet temperatures, A_{pv} represents the active area (m^2) of the PV cells, solar irradiation is given by G in W/m^2, and Δt is the duration of the experiment, respectively.

2.3.2. Photovoltaic Efficiency

The PV cell harnesses a fraction of the spectral photon energy to generate electricity. The light illuminated by the solar simulator is evenly distributed with gradual decay. Using one sun as the standard reference irradiance, the maximum power output and η_{el} were determined as follows:

$$\eta_{el} = \frac{I_{max}\, V_{max}}{A_{pv}\, G} \tag{2}$$

where I_{max} and V_{max} represent the current and voltage at the maximum power point (MPP). The η_{total} is used to evaluate the performance of the overall system and is given in Eq. (3).

$$\eta_{total} = \eta_{th} + \eta_{el} \tag{3}$$

2.3.3. Exergy Efficiency

Exergy efficiency (η_{ex}), derived from the second law of thermodynamics, optimizes energy use and adjusts distribution in integrated systems. Unlike energy efficiency, it assesses process irreversibility and energy quality. In PV/T modules, it closely depends on the nanofluid's operating temperature. Therefore, the electrically induced η_{ex} of passive PV/T system is given as:

$$\eta_{ex\,(el)} = \eta_{el} \tag{4}$$

but, for an active PV/T system, the $\eta_{ex\,(el)}$ is revised as the difference between PV power and necessary pumping power, i.e.,

$$\eta_{ex\,(el)} = \eta_{el} - \dot{E}_{pump} \tag{5}$$

where E_{pump} is the electrical power consumption of the pump and equals to,

$$\dot{E}_{pump} = \frac{\dot{m}\, \Delta P}{\rho\, \eta_p} \tag{6}$$

where η_p is the pump efficiency.

$$\eta_{ex\,(th)} = \left(1 - \frac{T_{amb}}{T_{nf}}\right) \eta_{th} \tag{7}$$

Overall,

$$\eta_{ex\,(total)} = \eta_{ex\,(el)} + \eta_{ex\,(th)} \tag{8}$$

2.3.4. Merit Function (MF)

The electrical and thermal outputs impact the system's economic performance. The *MF* serves as a key indicator of the hybrid NSS-PV/T system's economic efficiency and is determined as follows:

$$MF = \frac{\omega\, \eta_{el} + \eta_{th}}{\omega\, \eta_{el,0}} \tag{9}$$

where ω is the worth factor (ratio of the price of electricity to gas, which is usually considered ~ 3), and $\eta_{el,0}$ is the electric efficiency of the PV module without Au-ZnO/(W-EG) filter. The detailed uncertainty analysis and characterisation techniques are presented in the supplementary material.

3. Results and Discussion

3.1. Morphological and structural Analysis of ZnO NSs and Au$_{60\ \mathrm{nm}}$-ZnO composite

The Au-ZnO/water NF was characterised using UV-visible spectroscopy and Transmission Electron Microscopy (TEM). Transmittance was measured in a 10 mm quartz cuvette at a fixed concentration using a Perkin Elmer Lambda 950 spectrophotometer with a 2-D detector. TEM images of ZnO NSs and Au-NPs were captured using a FEI Tecnai G2 F30 S-Twin TEM at 300 kV, and the ZnO NSs crystal structure was analysed via Selected Area Electron Diffraction (SAED). NFs concentration was determined using a weight-to-volume ratio measured with a SHIMADZU AUW120D balance.

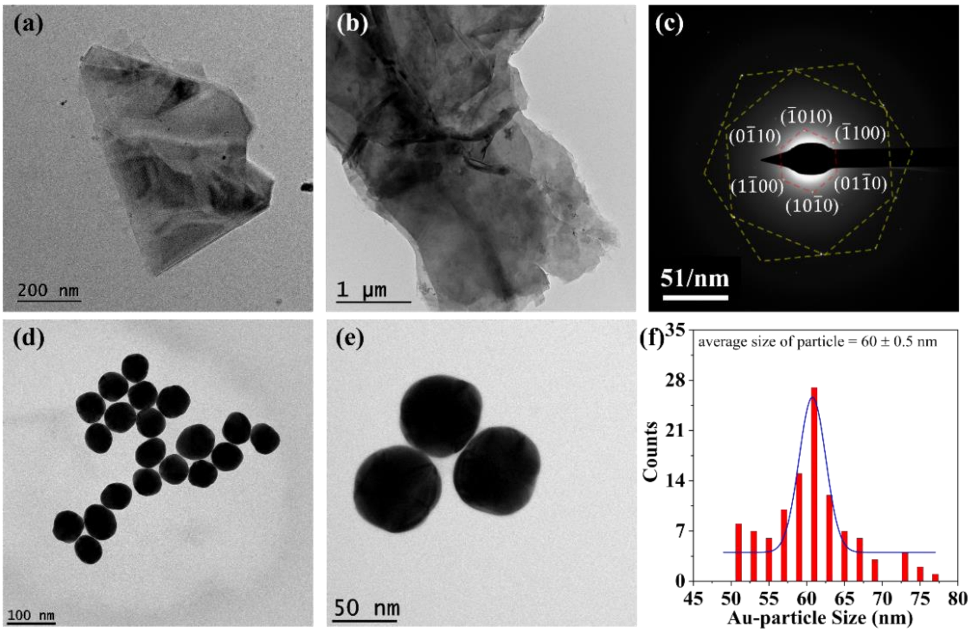

Fig. 3. Morphological Analysis of ZnO NSs and Au-NPs including (a-b) TEM images of ZnO NSs, (c) SAED pattern of ZnO NSs, (d-e) TEM images of Au-NPs, and (f) particle size distribution of Au-NPs.

The morphology of the Au-ZnO/(W-EG)-NFs, examined via TEM (Fig. 3), was achieved using a reagent-free electrophoretic synthesis combining anodic oxidation and electric-field-induced assembly. This method generates metal oxide quantum dots (QDs) through water electrolysis at the anode. The QDs, charged and dipolar due to the DC field, align and assemble into nanostructures near the cathode within ~30 min. For ZnO, 1 nm-thick, 4 nm-diameter QDs coalesce into 2-D nanoribbons and further into 2-D atomic nanostructures with high lateral-to-thickness ratios. The process minimises nonpolar facets, resulting in polar facet-dominated surfaces. This novel, a stable variant of ZnO NSs is governed by intrinsic surface polarity during electrophoretic assembly.

Fig. 3(a) and 3(b) depict TEM images of ZnO NSs synthesised via electrophoretic deposition, showing well-dispersed, sheet-like structures with lateral dimensions of 5-10 µm. Their high surface area enhances buoyancy and NFs stability. Longer synthesis times (> 5 h) lead to web-like structures under ambient lighting, which can be broken into uniformly dispersed NSs through 10 min of sonication. The formation of NSs arises from the inherent surface polarity of ZnO, facilitating their coalescence. Increased applied voltage enhances NF concentration by amplifying the electric field, promoting greater water ionisation, Zn oxidation, and alignment of Zn QDs into NSs.

The electrophoretic synthesis of ZnO NSs requires water as the primary solvent, as other solvents, such as ethylene glycol (EG), do not participate in the process. Electrode spacing influences NF stability; reducing the spacing from 2 cm to 1 cm increases NF concentration but causes ZnO NSs agglomeration due to limited dispersion space. ZnO NSs align with the electric field within the liquid volume, concentrating between electrodes and reducing fluid stability. While volume impacts overall NF concentration, the rate of NS formation is primarily governed by applied voltage and electrode spacing. The SAED pattern of ZnO NSs, shown in Fig. 3(c), confirms their crystalline nature. This pattern is generated when an electron beam of appropriate energy interacts with the crystal lattice, undergoing diffraction through atomic planes. Each diffraction spot corresponds to a specific family of lattice planes, providing a structural fingerprint. The distance of each spot from the centre is inversely proportional to the d-spacing of the corresponding planes. The SAED analysis, conducted using ImageJ software, indexed the ZnO NSs to a hexagonal wurtzite-type crystal structure consistent with the JCPDS card (ICSD collection code 067848). The lattice spacings align with (hkl) indices perpendicular to (001), as identified in the SAED pattern.

TEM images of Au-NPs (Fig. 3(d) and 3(e)) reveal that they are nearly spherical, with a calibrated diameter of approximately 60 nm. The size distribution (Fig. 3(f)), plotted after analysing a large number of particles, follows a Lorentzian fit, yielding an average particle size of 60 ± 5 nm. The images indicate that the Au-NPs are monodispersed, forming a uniform solution. ZnO NSs, with a lateral dimension of approximately 10 µm, were mixed with the spherical Au-NPs (60 ± 5 nm) to create a stable composite solution, combining the unique properties of both materials.

Primarily, X-ray diffraction (XRD) analysis was conducted to investigate the structural properties, crystallinity, and phase composition of the synthesised ZnO-NSs and the Au$_{60\text{ nm}}$-ZnO nanocomposite in the 2θ range of 20° to 70°. The characteristic XRD diffraction pattern of the pristine ZnO-NSs shown in Fig. 4 (black) exhibits a series of well-defined and intense diffraction peaks located at 2θ values of 31.86°, 34.39°, 36.20°, 47.48°, 56.59°, 62.86°, 66.35°, 67.92°, and 69.13°, which correspond to the crystallographic planes (100), (002), (101), (102), (110), (103), (200), (112), and (201), respectively. These reflections are in excellent agreement with the hexagonal wurtzite structure of ZnO (space group: $P6_3mc$, JCPDS No. 36-1451). The absence of any impurity peaks confirms the phase purity of the synthesised material. The sharpness and intensity of the peaks suggest that the ZnO nanosheets are well-crystallised with preferred orientation along the (101) plane.

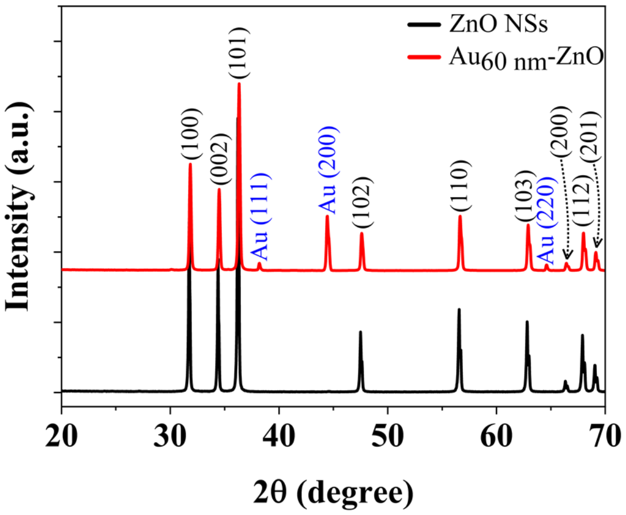

Fig. 4. Characteristic XRD diffraction patterns of bare ZnO NSs and Au60 nm-ZnO composite scanned between 2θ ranges from 20° to 70°.

Upon incorporation of Au nanoparticles (~ 60 nm), the XRD pattern of the Au$_{60\text{ nm}}$-ZnO nanocomposite retained the characteristic peaks of ZnO, confirming the structural integrity of the host ZnO NSs. In addition to the ZnO peaks, new diffraction peaks were observed at approximately 38.19°, 44.46°, and 64.61°, corresponding to the (111), (200), and (220) planes of face-centred cubic (fcc) Au, matching well with the JCPDS card no. 04-0784. The presence of these additional peaks confirms the successful decoration of ZnO with crystalline Au nanoparticles. These observations unequivocally confirm the successful formation of a Au$_{60}$

$_{nm}$-ZnO heterostructure, wherein both the semiconductor and metallic constituents retain their crystalline identities. The presence of Au does not introduce any detectable secondary or alloyed phases, as evidenced by the absence of additional impurity peaks, underscoring the structural purity of the nanocomposite.

Furthermore, a slight reduction in the intensity of ZnO peaks and marginal peak broadening was observed in the composite, which could be attributed to surface coverage of ZnO by Au nanoparticles, lattice strain due to interfacial interactions, or slight agglomeration effects. The crystallite size of Au calculated from the (111) reflection using the Scherrer equation was found to be approximately 55-60 nm, which closely matches the expected nanoparticle size, indicating minimal size distortion post-integration. This coexisting $Au_{60\ nm}$-ZnO configuration is anticipated to facilitate interfacial charge transfer processes due to favourable band alignment between the ZnO conduction band and the Fermi level of Au. This is crucial for applications in plasmon-enhanced PV/T spectral beam splitters, where metal-semiconductor interfaces play a pivotal role.

3.2. Optical Studies of the Au-ZnO/(W-EG) Nanofluids

The synergistic optical properties of the $Au_{60\ nm}$-ZnO/(W-EG)-NFs were assessed by measuring transmission spectra across the 250-1500 nm wavelength range, covering UV, visible, and NIR regions. As shown in Fig. 5(a), transmittance was influenced by reaction duration, applied voltage, and electrode spacing. Considering the spectral response of Si (700-1100 nm) and CdTe (450-860 nm) solar cells, high NF transmittance in these ranges is essential for high η_{el} [55]. $Au_{60\ nm}$-ZnO/(W-EG)-NFs demonstrated excellent transmittance in the UV and visible regions, highlighting their potential for solar applications. As visible in Fig. 5(b), the UV transmittance drop observed in all samples, compared to the water transmission spectrum, indicates ZnO formation. Among the samples, S9 exhibited the most significant UV transmittance reduction, followed by S11, though this was accompanied by a decrease in visible transmittance. Visible transmittance dropping below 80% could be mitigated by lowering the ZnO-NSs concentration in the $Au_{60\ nm}$-ZnO/(W-EG)-NF. Therefore, the S9 parameters were selected for further synthesis, characterization, and analysis using a water solvent assisted by enhanced NFs stability. This $Au_{60\ nm}$-ZnO/(W-EG)-NF demonstrated a notable UV transmittance reduction without affecting visible transmittance, outperforming ZnO/(W-EG)-NFs in UV blocking efficiency. Moreover, the $Au_{60\ nm}$/(W-EG)-NF exhibited a sharp transmittance drop below 700 nm, with nearly zero UV transmittance due to strong localised surface plasmon resonance (LSPR), as shown in Fig. 5(c).

Incorporating Au-NPs into ZnO resulted in a significant reduction in UV and visible transmittance in the $Au_{60\ nm}$-ZnO/(W-EG)-NF compared to bare ZnO/(W-EG)-NF. An absorption peak at 540 nm, attributed to the LSPR phenomenon of Au-NPs, was distinctly observed [56]. Au-NPs alone in water showed very low transmittance within the 250-540 nm range, making them highly suitable for PV/T spectral splitting applications. Although the ZnO nanosheets exhibit an expected strong UV absorption below 375 nm, the observed transmission spectrum shows reduced clarity of this effect due to quantum confinement-induced bandgap widening and diminished absorption cross-sections arising from the nanosheets' ultrathin geometry (~5 nm). Moreover, the prominent Au NPs LSPR at ~540 nm significantly influences and partially obscures ZnO's UV absorption features. However, combining ZnO-NSs with $Au_{60\ nm}$-NP suspension slightly increased UV transmittance compared to $Au_{60\ nm}$-NPs in water alone. The $Au_{60\ nm}$-ZnO/(W-EG)-NF spectrum displayed absorption peaks corresponding to ZnO and Au at 370 nm and 540 nm, respectively.

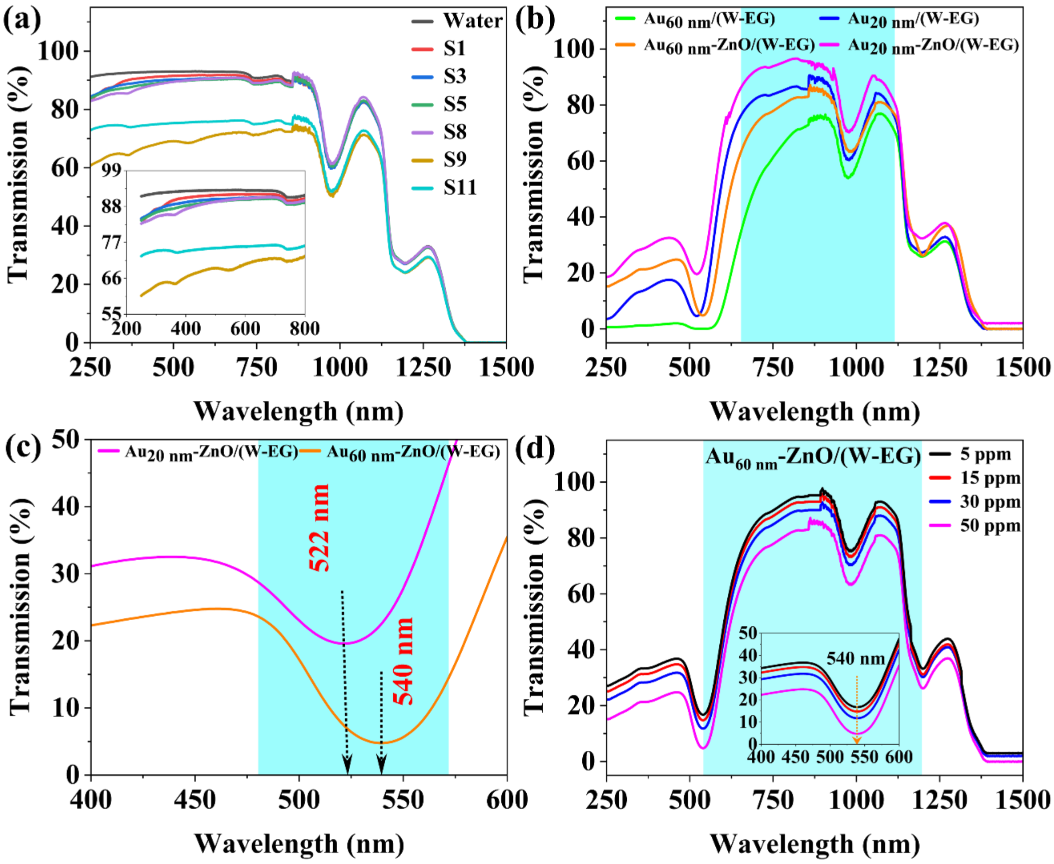

Fig. 5. UV-visible transmission studies in the range of 250 to 1500 nm highlight the effective utilization of $Au_{60\ nm}$-ZnO/(W-EG)-NFs. (a) the transmission of different NFs for optimization

study, (b) transmittance of various compositions of the NF such as $Au_{20\ nm}$/(W-EG), $Au_{60\ nm}$/(W-EG), $Au_{20\ nm}$-ZnO/(W-EG), and $Au_{60\ nm}$-ZnO/(W-EG), (c) absorption peak shifting in $Au_{60\ nm}$/(W-EG)-NFs after adding ZnO NSs, and (d) transmission spectra of $Au_{60\ nm}$-ZnO/(W-EG) NFs as a function of varying ppm levels of Au-NPs.

Additionally, Fig. 5(c) shows a ~ 4 nm shift in the LSPR peak between $Au_{60\ nm}$-ZnO/(W-EG)-NF and Au-NPs, attributed to strong interfacial coupling. Electron transfer from ZnO to Au, due to ZnO's higher conduction band relative to Au's Fermi level, causes Fermi level alignment and upward band bending. This alters charge density, broadening and shifting the LSPR peak. Upon LSPR excitation, hot carriers in Au transfer to ZnO's conduction band and relax to its valence band via photon emission (~ 3.3 eV), enabling wavelength down-conversion at the interface and agreeing well with the literature [57]. Further, transmission spectra of $Au_{60\ nm}$-ZnO/(W-EG)-NF were carried out in the wavelength range of 250 to 1500 nm, and shown in Fig. 5(d). As the concentration of the Au-NPs increases from 5 ppm to 50 ppm, the % transmission from the $Au_{60\ nm}$-ZnO/(W-EG)-NFs is also decreasing from ~ 97% to 87% and following similar trends.

Higher concentrations of Au-NPs lead to increased scattering of incident light due to their plasmonic nature. This scattering reduces the amount of light transmitted through the NF-medium, leading to reduced UV-visible transmission. Simultaneously, Au-NPs exhibit LSPR, which increases their ability to absorb light at specific wavelengths. Therefore, increasing Au-NP concentration increases the cumulative absorption within the medium hence reducing the transmitted light. Higher Au-NPs ppm levels in $Au_{60\ nm}$-ZnO/(W-EG)-NF, also increase the optical density of the medium, resulting in a longer effective optical path length and more light interaction with the nanoparticles. Furthermore, at elevated concentrations, there is a possibility of nanoparticle aggregation, forming larger clusters. These aggregates scatter and absorb light more efficiently than individual particles, amplifying the reduction in transmission. So, conclusively for an efficient PV/T spectral splitter, one should use a carefully balanced concentration of Au-NPs (in the range of 5-30 ppm) combined with ZnO in a water medium. This composition would provide optimal spectral splitting with high transmittance in the desired PV response range while ensuring stability and minimising excessive scattering.

3.3. Effect of Au-NP concentration and Solar Irradiance

$Au_{60\ nm}$-ZnO/(W-EG)-NF with Au-NP concentrations between 0 and 50 ppm demonstrated varying heat collection efficiencies due to the LSPR effect of photon energy absorption by Au-

NPs. Under illumination, the bulk fluid temperature increased at a diminishing rate as heat loss to the ambient environment rose with increasing temperature difference, eventually stabilising. This improvement was attributed to enhanced micro-convection and increased thermal conductivity due to nanoparticle-induced Brownian motion. The effect of the spectral filter on energy distribution was analysed using UV-visible spectroscopy for $Au_{60\ nm}$-ZnO/(W-EG) NF at various Au-NP concentrations, as shown in Fig. 5(d).

The nanofluids exhibited superior normalised transmission within the Si-PV cell bandgap. The LSPR absorption peak at ~ 540 nm remained unchanged across concentrations due to uniform particle size, and minimal scattering was observed due to the even dispersion of small particles in the fluid. Near-infrared absorption was attributed to water in the NF, while transmittance between 850 and 1250 nm decreased with higher nanoparticle concentrations due to an increased extinction factor, enabling greater solar energy storage in the nanofluid. The transmission properties of $Au_{60\ nm}$-ZnO/(W-EG) NF impact the energy reaching the PV module and its efficiency. While functioning as a selective absorption spectral splitter, $Au_{60\ nm}$-ZnO/(W-EG) NFs are suboptimal for the Si-PV cell bandgap as they absorb energy outside the cell's response range, reducing PV efficiency. However, they help maintain low operating temperatures (t_{opt}) for the PV module. The performance of the $Au_{60\ nm}$-ZnO/(W-EG) NF -PV/T system was evaluated based on η_{el}, η_{th}, and η_{total} as a function of the Au-NPs concentration (Fig. 6(a)). At the constant t_{opt}: 10 mm and $\dot{m}$: 6 mL/min, the increasing Au-NP concentration from 0 to 50 ppm improves η_{total} and η_{th} despite reduced η_{el}. At 50 ppm, the system achieved 76.24% η_{total} (η_{th}: 64.62%, η_{el}: 11.62%), showing 7.42 times enhanced η_{total} as compared to the 5-ppm concentrated $Au_{60\ nm}$-ZnO/(W-EG) NF having η_{total} :70.97% (η_{th} : 58.45%, η_{el}: 12.52%). As the Au-NP concentration increases, transmission decreases (Fig. 5(d)), leading to better light absorption and enhanced η_{th} due to improved heat retention and conductivity. However, this reduced transmission limits light reaching the PV module, resulting in a significant decrease in η_{el} (~ 7.19%). This reflects a trade-off between thermal and electrical performance in the system.

Alongside, the optimal results of a PV/T system with $Au_{60\ nm}$-ZnO/(W-EG) NF type spectral splitter depends on solar intensity (G), as evidenced by the performance trends across varying irradiance levels (0.4 to 1 kW/m^2), shown in Fig. 6(b). At lower G (400 W/m^2), the PV/T achieves its highest $\eta_{total}$of 77.66%, driven by a high $\eta_{th}$of 67.62% and a modest η_{el} of 10.04%. This occurs because lower G minimizes heat losses, allowing the $Au_{60\ nm}$-ZnO/(W-

EG)-NF to effectively capture thermal energy while maintaining PV cell temperatures for decent electrical output. As G increases to 1000 W/m^2, η_{th}drops to 60.31% due to greater heat losses and elevated temperatures despite the NF's cooling effect. However, η_{el} rises to 12.93%, as the NF mitigates PV cell temperature rise, and higher G pushes the PV cells closer to their maximum power point.

The η_{total}, however, decreases to 73.24%, as the η_{th} decline outweighs the electrical gain. This indicates that optimal performance, whether prioritizing η_{el}, η_{th}, or η_{total}, changes with *G*. For applications needing high thermal output, lower intensities (e.g., 400-600 W/m^2) are optimal, while high electrical output is favoured at higher intensities (e.g., 1000 W/m^2). The NF's role as a spectral splitter further complicates this dependency, as its heat absorption and cooling capacity vary with *G*. Thus, achieving optimal results requires tailoring the system design, such as adjusting nanofluids $\dot{m}$ or ppm level to the expected *G* range and the trade-off between thermal and electrical outputs for specific application needs.

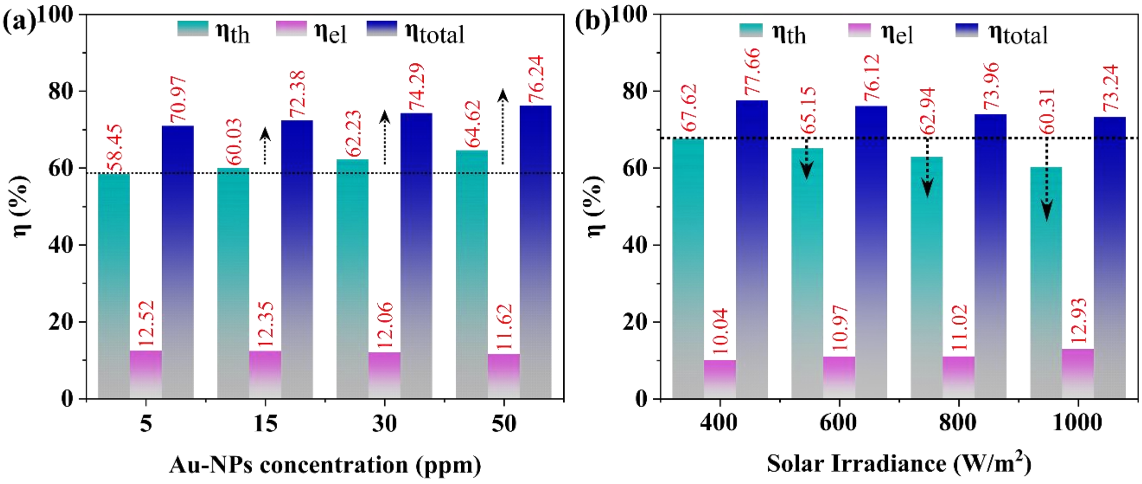

Fig. 6. Electrical (η_{el}), thermal (η_{th}), and total (η_{total}) PV performances of Au$_{60\ nm}$-ZnO/(W-EG)-NF-based spectral splitters (a) with respect to varying ppm levels of Au-NPs, and (b) under varying solar irradiance 400 to 1000 W/m^2.

3.4. Effect of mass flow rate ($\dot{m}$)

Optimising the Au-NPs concentration at 30 ppm and varying the $\dot{m}$ of Au$_{60\ nm}$-ZnO/(W-EG) NF from 2 mL/min to 6 mL/min at different t_{opt} revealed distinct trends in system performance, as shown in Fig. 7. As $\dot{m}$ increased, the η_{th} improved significantly, rising from 51.12% to 62.23% for t_{opt} = 10 mm and from 45.35% to 60.45% for t_{opt} = 30 mm. Simultaneously, the η_{el} demonstrated a slight but consistent increase, from 12.01% to 12.06% for t_{opt} = 10 mm and from 9.12% to 9.57% for t_{opt} = 30 mm. This improvement in η_{el} with increasing $\dot{m}$ contrasts with the declining η_{el} observed during nanoparticle concentration variation.

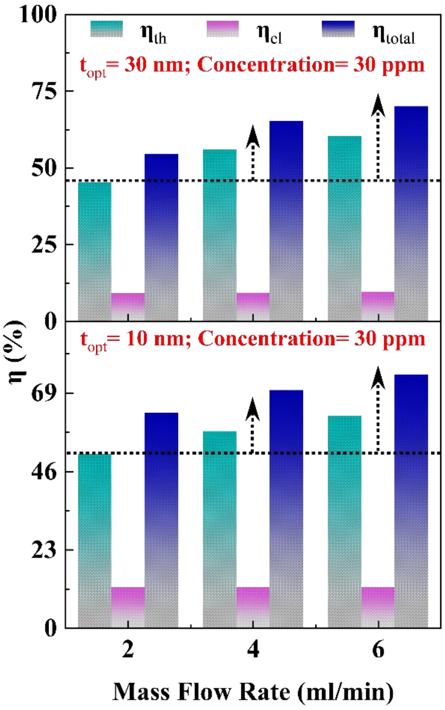

Fig. 7. Energy conversion efficiencies in the form of η_{el}, η_{th}, and η_{total} at varying $\dot{m}$ of $Au_{60\ nm}$-ZnO/(W-EG) NFs at constant ppm levels of Au-NPs (30 ppm) and two different t_{opt}'s of 10 mm and 30 mm.

The rising trend in η_{el} with increasing $\dot{m}$ can be attributed to enhanced cooling of the photovoltaic module due to higher heat dissipation from the nanofluid. Higher $\dot{m}$ reduce the bulk temperature of the $Au_{60\ nm}$-ZnO/(W-EG) NF filter and maintain the PV cell closer to its optimal t_{opt}, improving its electrical performance. Additionally, at a fixed concentration, the consistent optical properties of the nanofluid ensure sufficient transmittance to the PV cell, preventing significant spectral losses. The simultaneous increase in η_{el} is due to more efficient heat transfer facilitated by higher fluid velocity and greater convective cooling, resulting in improved overall thermal collection. This contrasts with concentration variation, where increasing nanoparticle concentration reduces transmittance and adversely affects η_{el}. Consequently, η_{total} reaches 76.24% at 50 ppm and 6 mL/min. However, the exergy efficiency (η_{ex}) decreases from 15.24% to 13.48%, reflecting lower outlet temperatures and reduced thermal energy quality, as governed by the Carnot factor ($1 - T_{amb}/T_{out}$).

3.5. Effect of Au-NPs diameter (d_{Au})

Furthermore, the effect of Au-NPs sizes on the energy conversion efficiencies (η_{th}, η_{el}, and η_{total}) was studied for two different ppm levels (5 ppm and 50 ppm) of Au-NPs at fixed t_{opt} = 10 mm of the Au-ZnO/(W-EG)-NF based PV/T spectral splitter. As shown in Fig. 8, all the η_{th}, η_{el}, and η_{total} were substantially decreasing with respect to the increasing Au-NPs diameter from 20 nm to 60 nm. Specifically, for 5 ppm Au-NPs concentration, the η_{th} decreases ~ 6.51% along with a 6.45% decrement in η_{el}, leading to the average 6.5% reduction in the overall performance. This indicates a significant sensitivity of smaller Au-NP concentrations to size variations. Similarly, Au_{50ppm}-ZnO/(W-EG) NF exhibits a similar trend as η_{th}, η_{el}, and η_{total} decreases by 3.07%, 3.10%, and 3.07%, respectively. Therefore, the less pronounced effect of larger ppm levels of Au-NPs suggests that higher concentrations mitigate the negative impact of larger particle sizes due to enhanced collective thermal effects.

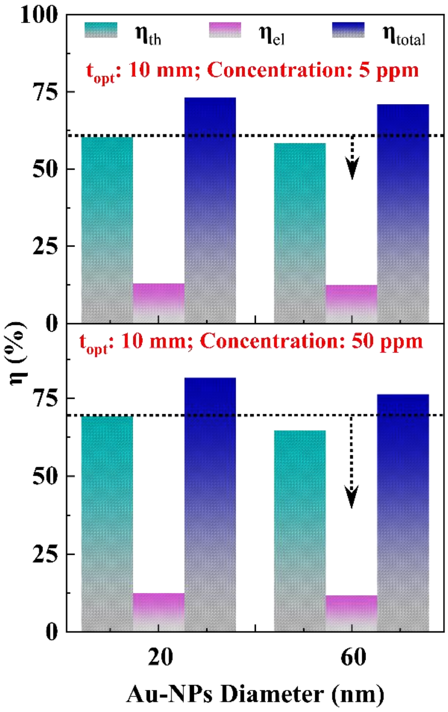

Fig. 8. Energy conversion efficiencies in the form of η_{el}, η_{th}, and η_{total} at varying d_{Au} (20 nm and 60 nm) in Au-ZnO/(W-EG) NFs at constant t_{opt}: 10mm and two different concentration (ppm) levels of Au-NPs which are 5 ppm and 50 ppm.

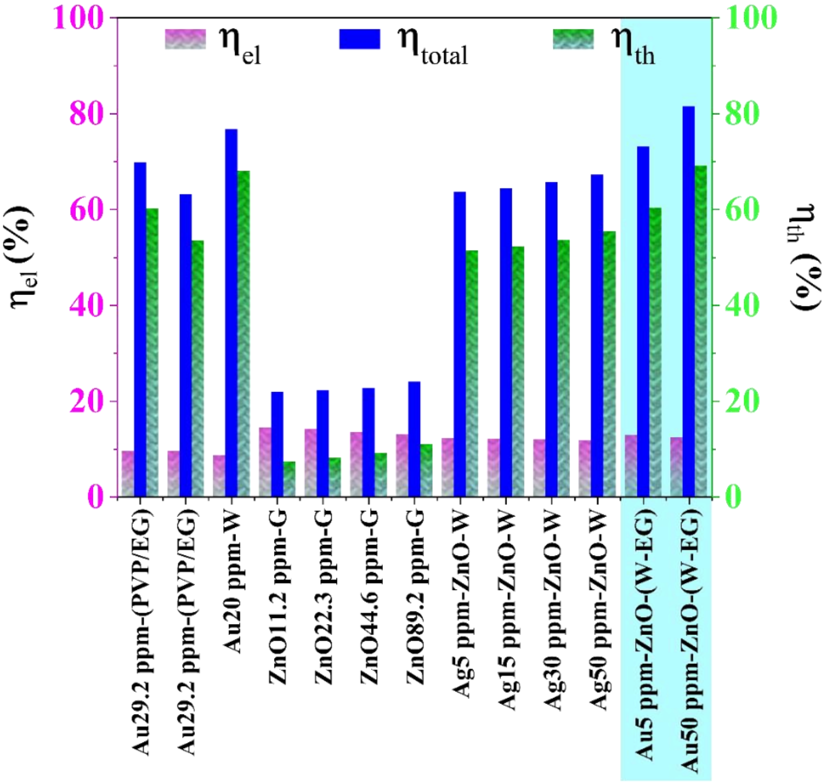

Fig. 9. Comparative PV and PT studies of various Au-NP and ZnO-based NFs using distinct liquid suspensions such as water, glycol, ethylene glycol, and mixtures [34,58,59].

The observed decrease in η_{th}, η_{el}, and η_{total} with increasing Au-NP diameter (from 20 nm to 60 nm) can be attributed to the reduced surface-area-to-volume ratio and diminished plasmonic effects of larger nanoparticles. Smaller Au-NPs exhibit stronger LSPR effects, enhancing light absorption and scattering in the nanofluid, which improves thermal and optical performance. As the diameter increases, the LSPR effect weakens, leading to reduced photon absorption and thermal conductivity, thereby diminishing the overall efficiency.

Further, a comparative study was performed with the available literature and concluded that this novel Au-ZnO/(W-EG) NF based SBS is the most promising solution for enhancing the performance of PV/T systems. However, there is no such study available with a similar composition, so we have compared our results with the literature available for Au, ZnO, or ZnO composites with other plasmonic materials. In 2023, Han *et al.* [58] optimised the Au-NF parameters for Si-PV cells, focusing on d_{NPs}, concentration, and t_{opt} to improve PV/T system performance. Surface-modified Au/W and Au/EG nanofluids with PVP or PEG coatings were prepared and tested for long-term stability under ambient storage, high-temperature heating, and solar radiation cycling. The optimal Au/W-NF, with d_{Au} of 20 nm, nanoparticle concentration of 49 ppm, and t_{opt} of 20 mm, achieved a MF of 1.367. Indoor flowing experiments showed that the mass flow rate had minimal impact on the PV performance of the Si-PV cell but negatively affected the η_{th} of the Au/(PVP-EG) NF-filtered PV/T system. When the $\dot{m}$ increased from 2 mL/min to 6 mL/min, the η_{th} dropped from 60.24% to 53.55%.

Recently, Li *et al.* [34] optimized Au/W-NF by controlling the NFs concentration and t_{opt} for PV/T application under extreme conditions. The result claims that at 75 ppm concentration and 20 mm t_{opt}, solar utilization efficiency was 88.5% with a *MF* of 2.48. The optimal 20 ppm concentration achieved 13.71% exergy efficiency. The NSS-assisted PV/T device reached 50 °C at 18 mm t_{opt}, with an η_{ex} of 12.77%, higher than at 22 mm due to reduced heat loss. In other work, the feasibility of using cost-effective ZnO/G-NF in spectral splitting CPV/T systems was experimentally verified. The ZnO/G-NF-based system showed a 3.8% increase in PV efficiency compared to the CPV cell. Its efficiency correlation coefficient (0.218) was 0.05 higher than Ag-SiO_2/W and 0.218 higher than water-polypyrrole-based systems. Again, η_{th} increased by 47% when ZnO nanoparticle concentration rose from 11.2 ppm to 89.2 ppm [59]. These results were graphically tabulated in Fig. 9 for a fair comparative study.

Moreover, in one of our studies based on plasmonic Ag-ZnO/W-NF SBS for indoor PV/T spectral splitters, we found that increasing NF-concentration reduced solar flux on the PV-cell, lowering η_{el} but improving η_{th}. The η_{el} increased with increasing *G*, while η_{th} decreased due to higher heat loss at higher temperature differentials. η_{el} remained stable with varying concentrations, *G*, and t_{opt}, with η_{total} dominated by η_{th} (65 ± 5%). Uncertainty analysis showed minor variations in η_{el} (~ 2.44%) and η_{th} (~ 2.07%). The optimal concentrations, G and t_{opt} for maximum performance were 50 ppm, 800-1000 W/m^2, and 30 mm, respectively, making Ag-ZnO nanofluid filters a cost-effective and sustainable option for PV/T systems.

Hence, Au-based NFs outperform Ag-based NFs in PV/T systems primarily due to their stronger plasmonic resonance and higher thermal conductivity, which enhance both light absorption and heat dissipation, leading to superior η_{el} and η_{th}. The higher plasmonic effect of Au allows better light conversion, while its better heat transfer properties help maintain the PV cell's temperature, improving overall η_{total}. In contrast, Ag-based NFs, though still effective, exhibit lower plasmonic resonance and thermal conductivity, resulting in comparatively lower performance. Moreover, Au's stability prevents oxidation, ensuring long-term durability, whereas Ag is more prone to oxidation, potentially reducing the nanofluid's longevity. Au-NPs are costlier than silver, making Au-based nanofluids a marginally expensive choice, while Ag-based NFs offer a cost-effective solution with relatively high performance, suitable for applications where budget is a constraint. In summary, Au-based NFs provide superior performance in PV/T systems but at a slightly higher cost, while Ag-based NF offer a more economical alternative with slightly lower efficiency. The choice depends on the balance between performance and cost.

3.6. Merit Function (MF) and Exergy Efficiency (η_{ex})

Further, the overall performance improvement was rigorously investigated through *MF* and exergy analysis of the designed PV/T system, as shown in Fig. 10. In the PV/T system employing $Au_{60\,nm}$-ZnO/(W-EG) NF as a spectral splitter, the observed trend of an increasing *MF* alongside a decreasing $\eta_{ex}$with rising $\dot{m}$ (2 to 6 mL/min) is both physically sound and experimentally plausible. The *MF*, often defined as a weighted sum of η_{el} and η_{th} (Eq. 9), rises from 1.793 to 2.025 as the $\dot{m}$ increases from 2 mL/min to 6 mL/min, reflecting enhanced system performance. This occurs because higher $\dot{m}$ improve convective heat transfer, reducing PV cell temperatures and boosting η_{el} due to the negative temperature coefficient of PV materials (e.g., -0.4% to -0.5%/°C for silicon).

Simultaneously, the $Au_{60\,nm}$-ZnO/(W-EG)-NF, acting as a spectral filter, absorbs more thermal energy from the infrared spectrum, increasing η_{th}, though the outlet temperature may drop slightly due to reduced residence time. The *MF*, prioritizing total energy output over quality, benefits from these gains, making its increase consistent with improved cooling and heat extraction. Conversely, η_{ex}, which measures the quality of energy output relative to solar input, decreases from 15.24% to 13.48% over the same flow rate range, revealing a thermodynamic trade-off. As shown in Eq. (5-8), the $\eta_{ex}$is calculated as the ratio of η_{el}, equal to electrical energy, and η_{th}, adjusted by the Carnot factor ($1-T_{amb}/T_{nf}$) to the solar exergy input. While higher $\dot{m}$ enhance η_{el} by lowering cell temperatures, they reduce the nanofluid's outlet temperature, diminishing η_{th} due to a lower Carnot factor. This shift toward producing more low-grade thermal energy outweighs the electrical exergy gain, driving the overall η_{ex} downward. Thus, the data underscores a key distinction: the merit function captures energy quantity, while exergy efficiency reflects energy quality, with $Au_{60\,nm}$-ZnO/(W-EG) NF based PV/T systems exhibiting this characteristic divergence as flow rates rise.

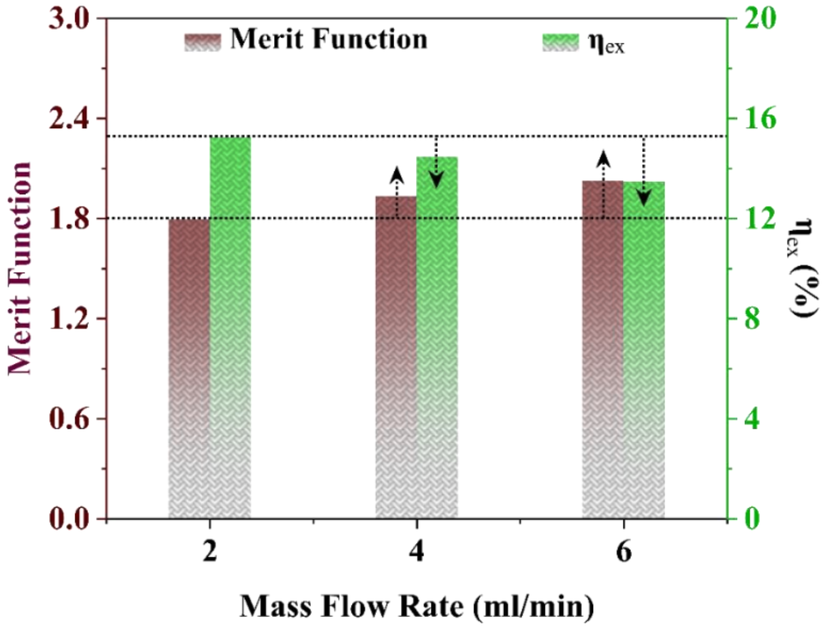

Fig. 10. Merit function and η_{ex} analysis as a function of $\dot{m}$ for Au$_{60\ \mathrm{nm}}$-ZnO/(W-EG)-NF with Au-NP size of 20 nm and 50 ppm concentration.

The contrasting trends indicate that while an increased nanofluid $\dot{m}$ enhances overall η_{th} and η_{el} (reflected in the *MF*), it reduces the quality of the extracted thermal energy due to lower temperature gradients. This suggests the presence of an optimal $\dot{\mathrm{m}}$, beyond which η_{ex} deteriorates due to excessive thermal dissipation and entropy generation.

3.7. Techno-economic Analysis of Au-ZnO/(W-EG) NFs

The production cost of Au-ZnO nanofluid ranges from 7.22-61.75 €/L (lab-scale) to 1.62-11.43 €/L (industrial-scale), primarily driven by Au precursor expenses (475-4750 €/kg). Stabilization and lifecycle costs contribute marginally (0.475-2.38 €/L and 1.14-9.13 €/L, respectively). Compared to conventional fluids (9.5×10^{-4}-19.00 €/L), Au-ZnO nanofluid is 10^{2}-10^{4} times costlier but offers 1.1 - 1.3 times improved thermal conductivity enhancement.

Further, typical synthesis cost, stabilization cost, lifecycle expenses, and comparative analysis against conventional NF-based spectral splitters are summarized in Table 2. Thus, the hybrid Au-ZnO/(W-EG) NF outperforms conventional nanofluids by integrating Au's localized surface plasmon resonance (LSPR) for tunable UV-vis absorption and ZnO's wide bandgap (3.37 eV) photocatalytic properties, enabling an overall 10-20% increase in PV/T system efficiency through optimized spectral beam splitting, surpassing the thermal conductivity and optical limitations of traditional fluids such as water, ethylene glycol, or oxide-based nanofluids.

Table 2. Techno-economic analysis of Au-ZnO/(W-EG)-NF-based PV/T spectral splitters against conventional nanofluids.

1. Material Synthesis Cost			
Components	**Description**	**Lab-Scale Cost (€/kg)**	**Industrial-Scale Cost (€/kg)**
ZnO precursor	$Zn(NO_3)_2$ or $Zn(CH_3COO)_2$	4.75-14.25	0.95-2.85
Au precursor	$HAuCl_4$	4.75×10^{2}-4.75×10^{3}	47.50-475.00
Base fluid	50:50 mixture, per L	0.475-2.38 (per L)	0.475-2.38 (per L)
Energy	Co-precipitation, 80-100°C, 2-4 h	0.95-4.75	0.095-0.475
Equipment	Reactors, stirrers	0.95-9.50	0.0475-0.475
Labor	Technician vs. automation	38.00-190.00	0.095-0.95
Total	**Sum of components**	**5.23×10^{2}-5.23×10^{3}**	**47.50-523.50**
2. Stabilization Cost			
Surfactants	PVP or CTAB, 0.1-1 g/L	0.0095-0.0475	0.0095-0.0475
Ultrasonication	500 W, 1-2 h vs. continuous flow	0.475-1.90	0.0475-0.19
pH Adjustment	HCl/NaOH for zeta potential	0.0095-0.0475	0.0095-0.0475
Total	**Sum of components**	**0.475-2.38**	**0.095-0.285**
3. Lifecycle Expenses			
Production (1% vol.)	10 g Au-ZnO per L	5.23-52.30	0.475-5.23
Base Fluid	Water/EG addition	0.95-4.75	0.95-4.75
Maintenance	Viscosity checks, re-stabilization	0.095-0.95	0.095-0.475
Disposal/Recovery	Filtration, waste management	0.95-4.75	0.095-0.95
Total	**Sum over 1 year**	**7.22-61.75**	**1.62-11.43**

4. Economic Viability Analysis

- **Break-even Scenario:** For a 1000 L system, conventional fluids cost 0.95-19,000 €, vs. 1,620-11,430 € for Au-ZnO nanofluid. A 10% efficiency gain must save >1,620-11,430 € over 1-3 years.
- **Example:** Energy at 0.095 €/kWh, 10,000 kWh saved annually (950 €/year), yields a payback period of 1.7-12 years. Viable in high-energy-cost or niche applications (e.g., solar, biomedical).

4. Conclusions

The hybrid Au-ZnO/(W-EG) NF demonstrates exceptional potential as a spectral beam splitter in PV/T systems, integrating the plasmonic properties of 60 ± 5 nm Au nanoparticles (LSPR peak: 540 nm) and the photocatalytic activity of ZnO nanosheets (UV absorption: 370 nm, wurtzite structure, JCPDS 067848) to achieve a 10-20% efficiency enhancement over conventional NFs. ZnO-NSs and Au-NPs synthesized via electrophoretic deposition (10 V, 11 h, 2 cm spacing) and citrate reduction, the NF exhibited an improved thermal conductivity and maintained colloidal stability for over 144 h (A/A_0 > 90%), surpassing ZnO/(W-EG) (<14 h) and Au-NP/W (<14 h). Optical studies revealed a tunable transmittance drop from 97% to 87% (250-1500 nm) with Au-NP concentrations increasing from 5 to 50 ppm, optimizing spectral splitting for Si-PV (700-1100 nm) and CdTe (450-860 nm) cells. Performance metrics under 1000 W/m^2 irradiance showed η_{total} rising from 70.97% (η_{th}: 58.45%, η_{el}: 12.52%) at 5 ppm to 76.24% (η_{th}: 64.62%, η_{el}: 11.62%) at 50 ppm, though η_{el} declined by 7.19% due to increased absorption. $\dot{m}$ optimization (2-6 mL/min) enhanced η_{th} from 51.12% to 62.23% and η_{el} from 12.01% to 12.06% (t_{opt}: 10 mm), while larger Au-NP diameters (20-60 nm) reduced η_{total} by 6.5% at 5 ppm and 3.07% at 50 ppm, reflecting diminished LSPR effects. The *MF* increased by 12.93% (1.793 to 2.025) with increasing $\dot{m}$ from 2 to 6 mL/min, driven by improved η_{th} and η_{el}, whereas η_{ex} decreased by 11.55% (15.24% to 13.48%), indicating a shift toward lower-quality thermal energy.

Techno-economic analysis estimated production costs at 6.80-60.38 €/L (lab-scale) and 1.14-9.03 €/L (industrial-scale), dominated by Au precursors (475-4750 €/kg), compared to conventional fluids (0.00095-4.75 €/L). A payback period of 1.5-12 years (950 €/year savings, 1000 L system) supports economic viability in high-energy-cost scenarios. Compared to literature (e.g., Au/W-NF: η_{total} = 88.5%, *MF* = 2.48; ZnO/G-NF: 3.8% η_{el} gain), the Au-ZnO/(W-EG)-NF excels in stability and spectral selectivity, offering a robust, scalable solution for efficient photo-harvesting in PV/T systems when Au content and $\dot{m}$ are optimized. Thus, a careful balance of nanoparticle concentration, size, and fluid flow rate is essential for optimising the overall performance of PV/T spectral splitter systems, where thermal efficiency can be enhanced without excessively compromising electrical output. These findings highlight the effectiveness of Au-NPs in optimising solar energy utilisation within integrated PV/T systems.

CRediT authorship contribution statement

Sandesh S Chougule: Conceptualisation, Data Curation, Formal analysis, Investigation, Methodology, Resources, Supervision, Validation, Writing-Original Draft & editing. **Bhagyashree A. Gaikwad:** Writing - Review & Editing, Validation, Formal Analysis. **Inbaoli A:** Writing - Review & Editing, Validation, Formal Analysis. **Anand Ajayan:** Formal Analysis, Visualization. **Sandip K. Saha:** Formal Analysis, **Patrice Estellé:** Formal Analysis.

Declaration of Interest Statement

The authors declare no competing financial conflict of interest.

Data availability statement

The data that support the findings of this study are available from the corresponding author upon reasonable request.

Acknowledgment

We express our gratitude to the Department of Science and Technology, India (DST), for their financial support (TAR/2020/000358) of this study. This work was also supported by a Marie Skłodowska-Curie Individual Fellowship under the European Union’s Horizon 2020 Research and Innovation Programme (Grant Agreement No. 101028904) and further funded by the European Union’s Horizon Europe Research and Innovation Programme (Grant Agreement No. 101152661). The authors are thankful to the central instrumentation facility of IISER Thiruvananthapuram for access to various characterisation facilities. For the purpose of Open Access, the authors have applied a CC BY public copyright license to any Author Accepted Manuscript version arising from this submission.

References

[1] A. Inbaoli, S.K.C. S, S.S. Chougule, C.N. Markides, S. Jayaraj, Enhanced electrolytic immersion cooling for thermal crisis mitigation in high-energy – density systems, Energy Convers Manag 300 (2024).

[2] S.S. Chougule, S.K. Sahu, Thermal Performance of Nanofluid Charged Heat Pipe With Phase Change Material for Electronics Cooling, J Electron Packag 137 (2015). https://doi.org/10.1115/1.4028994.

[3] P.O. Sharma, S.D. Barewar, S.S. Chougule, Experimental investigation of heat transfer enhancement in pool boiling using novel Ag/ZnO hybrid nanofluids, J Therm Anal Calorim 143 (2021) 1051–1061. https://doi.org/10.1007/s10973-020-09922-2.

[4] S. Nasri, M. Zamanifar, A. Naderipour, S.A. Nowdeh, H. Kamyab, Z. Abdul-Malek, Stability and dynamic analysis of a grid-connected environmentally friendly photovoltaic energy system, Environmental Science and Pollution Research 30 (2023) 71701–71713. https://doi.org/10.1007/s11356-021-15255-w.

[5] M.T. Chaichan, H.A. Kazem, A.H.A. Al-Waeli, K. Sopian, M.A. Fayad, W.H. Alawee, H.A. Dhahad, W.N.R.W. Isahak, A.A. Al-Amiery, Sand and Dust Storms' Impact on the Efficiency of the Photovoltaic Modules Installed in Baghdad: A Review Study with an Empirical Investigation, Energies (Basel) 16 (2023). https://doi.org/10.3390/en16093938.

[6] S.D. Barewar, M. Joshi, P.O. Sharma, P.S. Kalos, B. Bakthavatchalam, S.S. Chougule, K. Habib, S.K. Saha, Optimization of jet impingement heat transfer: A review on advanced techniques and parameters, Thermal Science and Engineering Progress 39 (2023) 101697. https://doi.org/https://doi.org/10.1016/j.tsep.2023.101697.

[7] A. Gupta, S.S. Chougule, S.K. Saha, Cooling of highly concentrated photovoltaic cells with confined jet impingement by introducing channel configurations, Renew Energy 237 (2024) 121600. https://doi.org/10.1016/j.renene.2024.121600.

[8] A. Ibrahim, M.Y. Othman, M.H. Ruslan, S. Mat, K. Sopian, Recent advances in flat plate photovoltaic/thermal (PV/T) solar collectors, Renewable and Sustainable Energy Reviews 15 (2011) 352–365. https://doi.org/10.1016/j.rser.2010.09.024.

[9] M. Modak, S.S. Chougule, S.K. Sahu, An Experimental Investigation on Heat Transfer Characteristics of Hot Surface by Using CuO–Water Nanofluids in Circular Jet Impingement Cooling, J Heat Transfer 140 (2017). https://doi.org/10.1115/1.4037396.

[10] S.K. Pathak, V. Sharma, S.S. Chougule, V. Goel, Prioritization of barriers to the development of renewable energy technologies in India using integrated Modified Delphi and AHP method, Sustainable Energy Technologies and Assessments 50 (2022) 101818. https://doi.org/https://doi.org/10.1016/j.seta.2021.101818.

[11] F. Hussain, M.Y.H. Othman, K. Sopian, B. Yatim, H. Ruslan, H. Othman, Design development and performance evaluation of photovoltaic/thermal (PV/T) air base solar collector, Renewable and Sustainable Energy Reviews 25 (2013) 431–441. https://doi.org/10.1016/j.rser.2013.04.014.

[12] B.G. Akinoglu, B. Tuncel, V. Badescu, Beyond 3rd generation solar cells and the full spectrum project. Recent advances and new emerging solar cells, Sustainable Energy Technologies and Assessments 46 (2021) 101287. https://doi.org/10.1016/j.seta.2021.101287.

[13] M. Modak, S. Srinivasan, K. Garg, S.S. Chougule, M.K. Agarwal, S.K. Sahu, Experimental investigation of heat transfer characteristics of the hot surface using Al2O3–water nanofluids, Chemical Engineering and Processing: Process Intensification 91 (2015) 104–113. https://doi.org/https://doi.org/10.1016/j.cep.2015.03.006.

[14] A.H.A. Al-Waeli, K. Sopian, H.A. Kazem, M.T. Chaichan, Photovoltaic/Thermal (PV/T) systems: Status and future prospects, Renewable and Sustainable Energy Reviews 77 (2017) 109–130. https://doi.org/10.1016/j.rser.2017.03.126.

[15] F. Crisostomo, R.A. Taylor, D. Surjadi, A. Mojiri, G. Rosengarten, E.R. Hawkes, Spectral splitting strategy and optical model for the development of a concentrating hybrid PV/T collector, Appl Energy 141 (2015) 238–246. https://doi.org/10.1016/j.apenergy.2014.12.044.

[16] G. Huang, S.R. Curt, K. Wang, C.N. Markides, Challenges and opportunities for nanomaterials in spectral splitting for high-performance hybrid solar photovoltaic-thermal applications: A review, Nano Materials Science 2 (2020) 183–203. https://doi.org/10.1016/j.nanoms.2020.03.008.

[17] F. Polito, G. Huang, C.N. Markides, A Building-Integrated Hybrid Photovoltaic-Thermal (PV-T) Window for Synergistic Light Management, Electricity and Heat Generation, Advanced Science 2408057 (2024) 1–13. https://doi.org/10.1002/advs.202408057.

[18] Y. Jia, G. Alva, G. Fang, Development and applications of photovoltaic–thermal systems: A review, Renewable and Sustainable Energy Reviews 102 (2019) 249–265. https://doi.org/10.1016/j.rser.2018.12.030.

[19] X. Zheng, M. Dong, Q. Li, Y. Liu, X. Di, X. Lu, J. Meng, Z. Li, High-Performance UV Photodetector via Energy Band Engineering and LSPR-Enhanced Pyro-Phototronic Effect in Au Decorated 2D-PbI2/1D-ZnO Heterojunction, Adv Opt Mater 12 (2024) 2303177. https://doi.org/https://doi.org/10.1002/adom.202303177.

[20] J. Meng, Q. Li, J. Huang, C. Pan, Z. Li, Self-powered photodetector for ultralow power density UV sensing, Nano Today 43 (2022) 101399. https://doi.org/https://doi.org/10.1016/j.nantod.2022.101399.

[21] M. Dong, X. Zheng, Q. Li, Y. Liu, X. Di, J. Meng, Z. Li, Multi-effect coupling enhanced self-powered heterojunction ultraviolet photodetector with ultra-low detection limit, Materials Today 74 (2024) 85–93. https://doi.org/https://doi.org/10.1016/j.mattod.2024.03.004.

[22] W. An, J. Zhang, T. Zhu, N. Gao, Investigation on a spectral splitting photovoltaic/thermal hybrid system based on polypyrrole nanofluid: Preliminary test, Renew Energy 86 (2016) 633–642. https://doi.org/10.1016/j.renene.2015.08.080.

[23] W. An, J. Wu, T. Zhu, Q. Zhu, Experimental investigation of a concentrating PV/T collector with Cu9S5 nanofluid spectral splitting filter, Appl Energy 184 (2016) 197–206. https://doi.org/10.1016/j.apenergy.2016.10.004.

[24] J. Jin, D. Jing, A novel liquid optical filter based on magnetic electrolyte nanofluids for hybrid photovoltaic/thermal solar collector application, Solar Energy 155 (2017) 51–61. https://doi.org/10.1016/j.solener.2017.06.030.

[25] L. Huaxu, W. Fuqiang, Z. Dong, C. Ziming, Z. Chuanxin, L. Bo, X. Huijin, Experimental investigation of cost-effective ZnO nanofluid based spectral splitting CPV/T system, Energy 194 (2020) 116913. https://doi.org/10.1016/j.energy.2020.116913.

[26] S.S. Chougule, A. Srivastava, G.G. Bolegave, B.A. Gaikwad, P.M. Shirage, C.N. Markides, Next-generation solar technologies: Unlocking the potential of Ag-ZnO hybrid nanofluids for enhanced spectral-splitting photovoltaic-thermal systems, Renew Energy 236 (2024) 121405. https://doi.org/10.1016/j.renene.2024.121405.

[27] S.A. Adam, X. Ju, Z. Zhang, J. Lin, M.M. Abd El-Samie, C. Xu, Effect of temperature on the stability and optical properties of SiO2-water nanofluids for hybrid

photovoltaic/thermal applications, Appl Therm Eng 175 (2020) 1–11. https://doi.org/10.1016/j.applthermaleng.2020.115394.

[28] A.S. Abdelrazik, F.A. Al-Sulaiman, R. Saidur, Optical behavior of a water/silver nanofluid and their influence on the performance of a photovoltaic-thermal collector, Solar Energy Materials and Solar Cells 201 (2019) 110054. https://doi.org/10.1016/j.solmat.2019.110054.

[29] A.S. Abdelrazik, K.H. Tan, N. Aslfattahi, R. Saidur, F.A. Al-Sulaiman, Optical properties and stability of water-based nanofluids mixed with reduced graphene oxide decorated with silver and energy performance investigation in hybrid photovoltaic/thermal solar systems, Int J Energy Res 44 (2020) 11487–11508. https://doi.org/10.1002/er.5770.

[30] S.D. Barewar, S. Tawri, S.S. Chougule, Experimental investigation of thermal conductivity and its ANN modeling for glycol-based Ag/ZnO hybrid nanofluids with low concentration, J Therm Anal Calorim 139 (2020) 1779–1790. https://doi.org/10.1007/s10973-019-08618-6.

[31] N.E. Hjerrild, S. Mesgari, F. Crisostomo, J.A. Scott, R. Amal, R.A. Taylor, Spectrum splitting using gold and silver nanofluids for photovoltaic/thermal collectors, Conference Record of the IEEE Photovoltaic Specialists Conference 2016-Novem (2016) 3518–3523. https://doi.org/10.1109/PVSC.2016.7750324.

[32] I. Hammami, N.M. Alabdallah, A. Al jomaa, M. kamoun, Gold nanoparticles: Synthesis properties and applications, J King Saud Univ Sci 33 (2021). https://doi.org/10.1016/j.jksus.2021.101560.

[33] T. Otanicar, J. Dale, M. Orosz, N. Brekke, D. DeJarnette, E. Tunkara, K. Roberts, P. Harikumar, Experimental evaluation of a prototype hybrid CPV/T system utilizing a nanoparticle fluid absorber at elevated temperatures, Appl Energy 228 (2018) 1531–1539. https://doi.org/10.1016/j.apenergy.2018.07.055.

[34] B. Li, W. Hong, H. Li, J. Lan, J. Zi, Optimized energy distribution management in the nanofluid-assisted photovoltaic/thermal system via exergy efficiency analysis, Energy 242 (2022) 123018. https://doi.org/10.1016/j.energy.2021.123018.

[35] F.L.J. Diniz, C.V.P. Vital, L.A. Gómez-Malagón, Parametric analysis of energy and exergy efficiencies of a hybrid PV/T system containing metallic nanofluids, Renew Energy 186 (2022) 51–65. https://doi.org/10.1016/j.renene.2021.12.151.

[36] X. Chen, P. Zhou, H. Yan, M. Chen, Systematically investigating solar absorption performance of plasmonic nanoparticles, Energy 216 (2021) 119254. https://doi.org/10.1016/j.energy.2020.119254.

[37] M. Chen, Y. He, J. Huang, J. Zhu, Investigation into Au nanofluids for solar photothermal conversion, Int J Heat Mass Transf 108 (2017) 1894–1900. https://doi.org/10.1016/j.ijheatmasstransfer.2017.01.005.

[38] N.E. Hjerrild, S. Mesgari, F. Crisostomo, J.A. Scott, R. Amal, R.A. Taylor, Hybrid PV/T enhancement using selectively absorbing Ag-SiO2/carbon nanofluids, Solar Energy Materials and Solar Cells 147 (2016) 281–287. https://doi.org/10.1016/j.solmat.2015.12.010.

[39] Y. He, Y. Hu, H. Li, An Ag@TiO2/ethylene glycol/water solution as a nanofluid-based beam splitter for photovoltaic/thermal applications in cold regions, Energy Convers Manag 198 (2019) 111838. https://doi.org/10.1016/j.enconman.2019.111838.

[40] W. An, L. Chen, T. Liu, Y. Qin, Enhanced solar distillation by nanofluid-based spectral splitting PV/T technique: Preliminary experiment, Solar Energy 176 (2018) 146–156. https://doi.org/10.1016/j.solener.2018.10.029.

[41] X. Yu, Y. Xuan, Investigation on thermo-optical properties of CuO/Ag plasmonic nanofluids, Solar Energy 160 (2018) 200–207. https://doi.org/10.1016/j.solener.2017.12.007.

[42] X. Han, X. Chen, Q. Wang, S.M. Alelyani, J. Qu, Investigation of CoSO4-based Ag nanofluids as spectral beam splitters for hybrid PV/T applications, Solar Energy 177 (2019) 387–394. https://doi.org/10.1016/j.solener.2018.11.037.

[43] L. Huaxu, W. Fuqiang, Z. Dong, C. Ziming, Z. Chuanxin, L. Bo, X. Huijin, Experimental investigation of cost-effective ZnO nanofluid based spectral splitting CPV/T system, Energy 194 (2020) 116913. https://doi.org/10.1016/j.energy.2020.116913.

[44] X. Han, X. Chen, Y. Sun, J. Qu. Performance improvement of a PV/T system utilizing Ag/CoSO4-propylene glycol nanofluid optical filter. Energy 2020;192:116611. https://doi.org/https://doi.org/10.1016/j.energy.2019.116611.

[45] J. Huang, X. Han, X. Zhao, C. Meng. Facile preparation of core-shell Ag@SiO2 nanoparticles and their application in spectrally splitting PV/T systems. Energy 2021;215:119111. https://doi.org/https://doi.org/10.1016/j.energy.2020.119111.

[46] X. Ju, H. Liu, M. Pei, W. Li, J. Lin, D. Liu, et al. Multi-parameter study and genetic algorithm integrated optimization for a nanofluid-based photovoltaic/thermal system. Energy 2023;267:126528. https://doi.org/https://doi.org/10.1016/j.energy.2022.126528.

[47] AS. Abdelrazik, R. Saidur, FA. Al-Sulaiman. Investigation of the performance of a hybrid PV/thermal system using water/silver nanofluid-based optical filter. Energy 2021;215:119172. https://doi.org/https://doi.org/10.1016/j.energy.2020.119172.

[48] O. Elharoun, M. Tawfik, II. El-Sharkawy, E. Zeidan. Experimental investigation of photovoltaic performance with compound parabolic solar concentrator and fluid spectral filter. Energy 2023;278:127848. https://doi.org/https://doi.org/10.1016/j.energy.2023.127848.

[49] Y. Xiao, W. Tian, L. Yu, M. Chen, X. Zheng, G. Qin. Tunable optical properties of ATO-CuO hybrid nanofluids and the application as spectral beam splitters. Energy 2024;289:129964. https://doi.org/https://doi.org/10.1016/j.energy.2023.129964.

[50] C. Hou, M. Zhang, T. Kasama, C. Engelbrekt, L. Zhang, H. Wang, Q. Chi, Reagent-Free Synthesis and Plasmonic Antioxidation of Unique Nanostructured Metal–Metal Oxide Core–Shell Microfibers, Advanced Materials 28 (2016) 4097–4104. https://doi.org/10.1002/adma.201505990.

[51] X. Zhao, X. Han, Y. Yao, J. Huang, Stability investigation of propylene glycol-based Ag@SiO2 nanofluids and their performance in spectral splitting photovoltaic/thermal systems, Energy 238 (2022) 122040. https://doi.org/10.1016/j.energy.2021.122040.

[52] H. Tyagi, A. Kushwaha, A. Kumar, M. Aslam, A Facile pH Controlled Citrate-Based Reduction Method for Gold Nanoparticle Synthesis at Room Temperature, Nanoscale Res Lett 11 (2016). https://doi.org/10.1186/s11671-016-1576-5.

[53] C. Hou, M. Zhang, L. Zhang, Y. Tang, H. Wang, Q. Chi, Reagent-Free Electrophoretic Synthesis of Few-Atom-Thick Metal Oxide Nanosheets, Chemistry of Materials 29 (2017) 1439–1446. https://doi.org/10.1021/acs.chemmater.7b00188.

[54] G.S. Smith, Human color vision and the unsaturated blue color of the daytime sky, Am J Phys 73 (2005) 590–597. https://doi.org/10.1119/1.1858479.

[55] G. Huang, K. Wang, S.R. Curt, B. Franchetti, I. Pesmazoglou, C.N. Markides, Performance analysis of fluid-based spectralsplitting hybrid photovoltaic-thermal solar collectors, ECOS 2020 - Proceedings of the 33rd International Conference on Efficiency, Cost, Optimization, Simulation and Environmental Impact of Energy Systems (2020) 1248–1259.

[56] A. Furube, S. Hashimoto, Insight into plasmonic hot-electron transfer and plasmon molecular drive: new dimensions in energy conversion and nanofabrication, NPG Asia Mater 9 (2017) e454. https://doi.org/10.1038/am.2017.191.

[57] K.N. Prajapati, B. Johns, K. Bandopadhyay, S.R.P. Silva, J. Mitra, Interaction of ZnO nanorods with plasmonic metal nanoparticles and semiconductor quantum dots, Journal of Chemical Physics 152 (2020). https://doi.org/10.1063/1.5138944.

[58] X. Han, Y. Yao, X. Zhao, J. Huang, A.A. Khosa, Investigations of stable surface-modified gold nanofluids optical filters based on optical optimization for photovoltaic/thermal systems, Sustainable Energy Technologies and Assessments 57 (2023) 103203. https://doi.org/10.1016/j.seta.2023.103203.

[59] L. Huaxu, W. Fuqiang, Z. Dong, C. Ziming, Z. Chuanxin, L. Bo, X. Huijin, Experimental investigation of cost-effective ZnO nanofluid based spectral splitting CPV/T system, Energy 194 (2020) 116913. https://doi.org/10.1016/j.energy.2020.116913.

Declaration of Interest Statement:

The authors declare no competing financial conflict of interest.